



Revealing the synergistic mechanism of generation, release, migration and utilization of reactive oxygen species through tailoring the d-band in metal organic frameworks for water purification

Dongya Li^{a,d}, Shiyu Zuo^b, Jinquan Wan^{b,c}, Yan Wang^{b,*}, Zeyu Guan^a, Zhicheng Yan^b, Fan Yang^e

^a School of Environmental Engineering, Wuhan Textile University, Wuhan, China

^b School of Environment and Energy, South China University of Technology, Guangzhou, China

^c Guangdong Plant Fiber High-Valued Cleaning Utilization Engineering Technology Research Center, Guangzhou, China

^d Engineering Research Center Clean Production of Textile Dyeing and Printing, Ministry of Education, Wuhan, China

^e School of Mathematical and Physical Sciences, Wuhan Textile University, Wuhan, China

ARTICLE INFO

Keywords:

Electronic structure
d-band center
Interfacial micro electric field
Reactive oxygen species
Directional migration

ABSTRACT

Reactive oxygen species (ROS) play important roles in environmental, chemical and biological fields, but the controlled release and migration of ROS remain a major challenge. Here, a highly efficient catalyst (Cu-MIL-101 (Fe)) by modifying the electronic structure was designed. The orbital hybridization achieves a deep optimization of the d-band (d band center shifted from -1.01 eV to -1.32 eV), which reduces bonding and antibonding orbitals energy levels, thus promoting release of $\text{SO}_4^{\cdot-}$. More importantly, the interfacial micro-electric field (IMEF) formed by the intramolecular charge offset mediates the directional migration of $\text{SO}_4^{\cdot-}$ from Fe sites to Cu sites. These properties endow the catalyst with high-efficiency $\text{SO}_4^{\cdot-}$ generation, rapid release, directional migration and utilization, with a 4.3-fold increase in effective oxidant utilization over Fe^{2+} (from 17.12% to 73.54%). This study highlights a catalytic strategy for efficient ROS generation, release, migration and utilization for a wide range of potential applications including environmental remediation.

1. Introduction

Aromatic pollutants (AP) in the aqueous environment are a class of compounds with stable aromatic ring structures [1–3]. Such pollutants are often detected in natural water bodies and wastewater treatment plant drainage at concentrations ranging from ng/L to $\mu\text{g/L}$. However, numerous studies have confirmed that these trace amounts of APs have adverse effects on ecosystems and human health due to their toxic and harmful properties, refractory biodegradation, and easy bio-accumulation and biomagnification [4]. However, the current conventional water treatment process mainly aims at the pollutants (easily degradable organic matter, nutrient substances, pathogens, etc.) with a large proportion of the pollution load in the wastewater. There is no specific design for the removal of AP. So AP is often regarded as an inert chemical oxygen demand (COD) continuously discharged to the receiving water body that accumulates in the environment and entered into the natural and social cycle of water, posing potential

environmental and human health risks [5,6]. Therefore, there is an urgent need for a cost-effective technology to efficiently eliminate of AP from water.

A heterogeneous advanced oxidation process (AOPs) based on PS generates a strong oxidizing $\text{SO}_4^{\cdot-}$, which effectively degrades AP by destroying the aromatic ring through electron transfer [7,8]. However, the low concentration of pollutants in the actual aqueous environment and the interference of impurities such as humic substances and inorganic salts make the effective collision probability between $\text{SO}_4^{\cdot-}$ and aromatic pollutants low, leading to the inability to preferentially remove the more harmful aromatic pollutants, low removal rate, and the waste of large amounts of oxidant [9,10]. To effectively treat trace APs in real water environments, efficient selective treatment methods need to be developed.

Targeted recognition and degradation/separation methodology are developed for the removal of specific pollutants in complicated aqueous environments [9,10]. Surface molecular imprinting (SMIP) can

* Corresponding author.

E-mail address: yanwang@scut.edu.cn (Y. Wang).

<https://doi.org/10.1016/j.apcatb.2023.122507>

Received 17 November 2022; Received in revised form 9 January 2023; Accepted 20 February 2023

Available online 21 February 2023

0926-3373/© 2023 Elsevier B.V. All rights reserved.

specifically identify target pollutants in complex environments and selectively bind through specific spatial structures and interactions, thereby achieving preferential and efficient removal of target pollutants [11–13]. However, there are still two critical issues that need addressing. First, the SMIP layer hinders the generation and mass transfer of reactive oxygen species (ROS). The active sites of the catalyst could be covered by the surface molecular imprinting, which leads to less exposure to active sites and poor ROS generation. In addition, the disordered and random migration of an outsized quantity of SO_4^- might result in inefficient utilization of SO_4^- , which cannot guarantee a high removal rate of pollutants [14–16]. Wan et al. created 3-dimension (3D) molecular imprints, that synergistically confine pollutants and SO_4^- in nanopores through the template effect and spatial confinement, thereby improving SO_4^- mass transfer and pollutant removal efficiency [17]. However, increasing the concentration of material in the nanopore and decreasing the mass transfer distance may not only increase the collision of SO_4^- with pollutants, but also the collision of SO_4^- with SO_4^- leading to self-quenching. The high degradation efficiency of pollutants is still accompanied by the high consumption of oxidants. Huang's group and previous studies by our group have shown that IMEF could selectively accelerate specific reactions by exerting directional forces on ions [18, 19]. SO_4^- is a typically charged ion. If an IMEF can be constructed on the catalyst interface, the SO_4^- will be enforced to migrate directionally based on the action of the electric field. SO_4^- self-quenching caused by the excessive local concentration can be avoided, and promote the interaction with response to pollutants [19].

However, the specific recognition sites fabricated on the catalysts are only used for pollutants adsorbing and accumulating. There is no gain effect on the catalytic reaction. Lyu's work found that cation- π interactions can adsorb and accumulate AP on metal cations, which may change the electronic energy state of the AP, causing π -electron delocalization (reducing π -electron delocalization energy) and thus leading to "activation" of the pollutant [20]. However, the stable construction of metal cation- π interaction is a challenge to sustainably induce pollutant adsorption on catalyst surfaces. Based on the good catalytic and electrochemical properties of IMEF, it can provide charge cycling to induce π -electron delocalization, form stable metal cation- π interactions, and promote electron transfer to enhance catalytic reactions.

Previous studies have shown that optimizing the electronic structure of catalysts would have unexpected effects. However, it is unclear whether optimization of the electronic structure can improve ROS release and migration. MIL-101 is considered a promising water purification material due to its adjustable and ordered voids [21–23]. Here, we design high-performance heterogeneous catalysts by improving the electronic structure of MIL-101(Fe) through Cu modification. The composition, morphology, and electronic structure of the catalyst were studied. Based on experimental and theoretical calculations, Cu-Fe orbital hybridization improves the metallicity of the catalyst, thereby enhancing electron mobility. Moreover, the broadening of the d occupied orbital distribution is more discrete, resulting in a downward shift of the d-band center, which is beneficial to the desorption of ROS and promotes the release of SO_4^- . After rapid release, directional migration of SO_4^- under the action of IMEF formed by intramolecular charge shift. A kinetic model was established based on the operating conditions to evaluate the performance of Cu-MIL-101(Fe) in regulating ROS generation, release and migration with AP as the target molecule. According to two-dimensional Fourier transform infrared correlation spectroscopy (2D-FTIR-COS), electronic density of states, molecular structure calculations, etc., to clarify the molecular mechanism of SO_4^- release and directional migration, for the efficient generation and release of ROS in heterogeneous catalysis and migration provide a scientific basis.

2. Experiment

2.1. Material preparation

1.08 g $\text{FeCl}_3 \cdot 5\text{H}_2\text{O}$ and 0.66 g 1,4-dicarboxybenzene (H_2BDC) were stirred and mixed in 30 ml N, N-dimethylformamide (DMF), then transferred to a Teflon-lined autoclave reactor and heated at 110 °C for 20 h. The resulting product was washed as a yellow powder. The yellow powder and CuCl were stirred and mixed in methanol solution according to a certain proportion, and at the same time heated to 70 °C, stirred, and evaporated to dryness. The obtained product was washed to obtain Cu-MIL-101(Fe). According to different proportions, they are recorded as MIL-101(Fe) (10:0), Cu-MIL-101(Fe)-1 (10:1), Cu-MIL-101(Fe)-2 (10:2), Cu-MIL-101(Fe)-3 (10:3), Cu-MIL-101(Fe)-4 (10:4), Cu-MIL-101(Fe)-5 (10:6). The Cat in manuscripts usually refers to Cu-MIL-101(Fe)-5.

2.2. Method

The reagents are described in the Text. S1.

The experimental procedure is described in the Text. S2 and Table S1.

Characterization and analysis methods are described in the Text. S3–5.

The density functional theory (DFT) calculation method is described in the Text. S6.

3. Results and discussion

3.1. Structure and properties

MIL-101(Fe) is an octahedral structure coordinated by Fe and H_2BDC . The schematic diagram of Cu surface doping MIL-101(Fe) is shown in Fig. 1a. Its structure was investigated by DFT calculations (Fig. S1). Due to the difference in electron-absorbing ability and surrounding electron density, the electrons of Fe and C may shift towards Cu. The structure optimization shows that the Fe-O bond length changes from 1.868 Å to 1.872 Å. This suggests that Cu doping may lead to the elongated Fe-O covalent bond, which could endow Fe with a stronger ability to drag electrons from O. The enlarged Fe-O bond could reduce the electron transfer energy barrier and promote catalytic behavior [24]. X-ray diffraction (XRD) spectrum shows characteristic peaks ascribed to MIL-101(Fe) (Fig. 1b). It is indicated that Cu surface doping did not significantly alter MIL-101(Fe) [25]. The spindle-like morphology also confirmed the main structure of MIL-101(Fe) (Fig. S2a). Elemental mapping shows that Cu doping is mainly on the surface rather than bulk doping (Fig. S2b). X-ray photoelectron spectroscopy (XPS) confirmed the presence of Cu in Cu-MIL-101(Fe) (Fig. S2c). These results preliminarily indicate the formation of Cu-doped MIL-101(Fe) catalyst (Cu-MIL-101(Fe)).

The Fourier transform infrared (FTIR) spectroscopy shows the characteristics of Fe-MOF (Fig. 1c). The characteristic peak at 554 cm^{-1} is assigned to Fe-O (Fe-MOF) [26]. The characteristic peaks at about 1000 cm^{-1} to 1600 cm^{-1} are attributed to organic ligands such as -COOH, C=O, -OH of FeMOF, respectively [27,28]. The characteristic peak of Cu-O (480 cm^{-1}) was detected and its intensity gradually increased with the increase of Cu doping amount. It is demonstrated that Cu was introduced in forming the Cu-O bond in MIL-101(Fe), which is consistent with the DFT-optimized structure shown in Fig. 1a [29]. To further explore the process of Cu doping on MIL-101(Fe), a 2D-COS was performed based on one-dimensional FTIR spectroscopy [30,31]. In the synchronous spectrum, four auto-peaks were observed at 480 cm^{-1} , 554 cm^{-1} , 1390 cm^{-1} , and 1601 cm^{-1} corresponding to Cu-O, Fe-O, -COOH, and C=O, respectively (Fig. 1d). It is demonstrated that the peak intensities of Cu-O were increased with the decreasing of Fe-O and organic ligands in Cu-MIL-101(Fe). In addition, a negative cross-peak

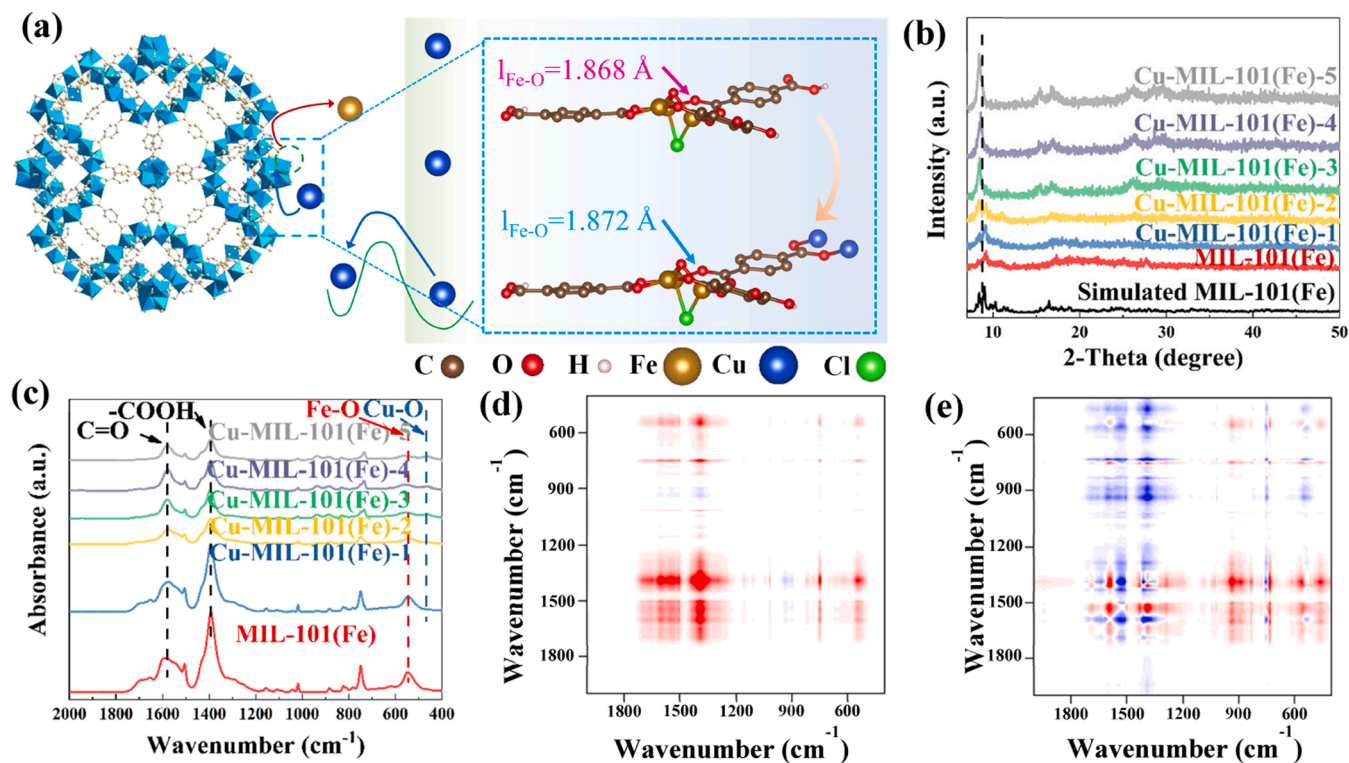


Fig. 1. (a) Schematic diagram of preparation and structural optimization model of Cu-MIL-101(Fe); (b) XRD and (c) FTIR of Cu-MIL-101(Fe); (d) synchronous and (e) asynchronous spectra of 2D-FTIR-COS.

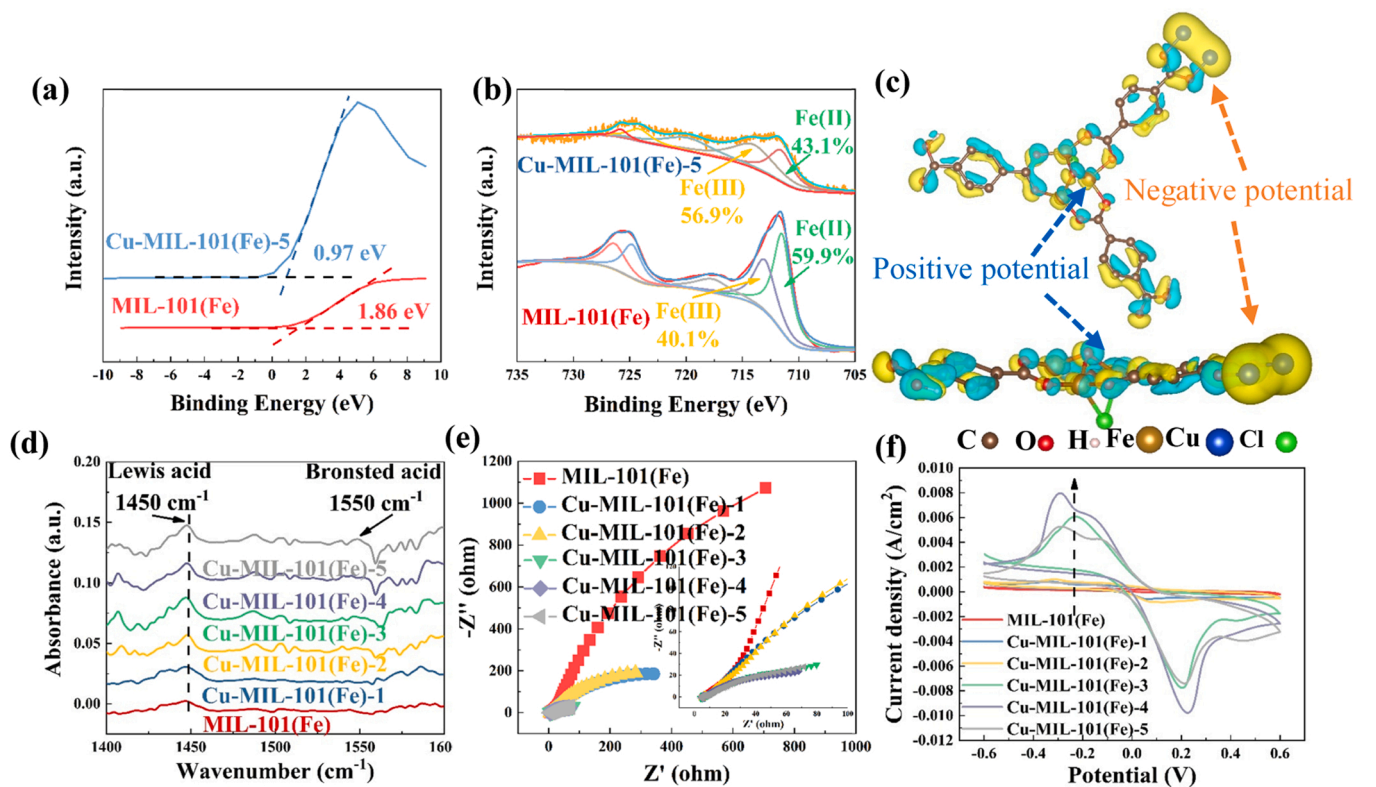


Fig. 2. (a) XPS VB of MIL-101(Fe) and Cu-MIL-101(Fe); (b) XPS Fe2p of MIL-101(Fe) and Cu-MIL-101(Fe); (c) differential charge density of Cu-MIL-101(Fe); (d) pyridine IR of MIL-101(Fe) and Cu-MIL-101(Fe); (e) EIS of Cu-MIL-101(Fe); (f) CV of Cu-MIL-101(Fe).

was observed in (480, 554), which indicated that Cu-O and Fe-O changes tended to be opposite in this process. This result also directly confirms the substitution of Cu-O for Fe-O in MIL-101(Fe). According to Noda Yoshiyo's rule, asynchronous spectroscopy could reveal the sequence of changes in the process. As shown in Fig. 1e and Table S2, asynchronous spectra are antisymmetric about the diagonal and there are no auto-peaks are shown. Some negative cross-peak signals ($\times 1480$) are observed in Fig. 1e. These indicate that the Fe-O on MIL-101(Fe) is fractured, and then Cu-O is formed by substituting Fe with Cu in Cu-MIL-101(Fe).

Cu doping not only leads to structural changes but also affects the electronic structure, which profoundly changes the electronic properties and catalytic behavior of MIL-101(Fe). The highest occupied molecular orbit (HOMO) of MIL-101(Fe) and Cu-MIL-101(Fe)-5 was determined by XPS VB which is shown in Fig. 2a. It shows that the HOMO level changed from 3.36 eV to 2.14 eV after Cu doping. It demonstrated that the electron of Cu-MIL-101(Fe)-5 escapes more easily than MIL-101(Fe), which is favorable for catalytic reduction. The changes of Cu, Fe and C 1s were also analyzed according to the XPS spectrum. The Cu 2p results show that the coexistence of Cu(I) and Cu(II) with an average valence of 1.36 (Fig. S3a) and average valence of Fe increased from 2.56 eV to 2.87 eV after doping with Cu (Fig. 2b). The C=O electron density of organic ligands was reduced (Fig. S3b). Specifically, the electrons are preferring to transfer from Fe and C to Cu, thereby forming Fe high-potential sites and Cu low-potential sites. This creates a potential difference (electric field) between Fe/Cu.

The changes in electronic structure and density were further explored by DFT. It is illustrated that the electron densities of Fe and C decreased with the increase of Cu in differential charge densities (Fig. 2c) [32,33]. And trigger electron delocalization of the Fe site, endowing it with high conductivity and low energy barrier, which may be beneficial to catalyze PS. The bader charge analysis also showed a decrease in the electron density of Fe and C (Fig. S3c). Due to the potential difference between Cu/Fe, the galvanic cell-like model was adapted to evaluate the electric field effect of Cu-MIL-101(Fe). Hereby, Fe, Cu and Fe-O-C-O-Cu (Fe...Cu) can be treated as the positive potential, negative potential, electronic bond bridge. Therefore, the IMEF of Cu-MIL-101(Fe) is lead to be formed. Based on the galvanic cell-like model, the IMEF on Cu-MIL-101(Fe) is divided into DIEF and DEEF. DEEF on Fe...Cu bonds facilitate electron transport. DIEF near the surface could mediate interfacial ion directional migration. The electric field forces exert on localized electrons and charged ions could improve the catalytic behavior of Cu-MIL-101(Fe).

The properties and electrochemical performance of Cu-MIL-101(Fe) may vary due to the effect of electronic structure optimization and IMEF. The Lewis acid sites of Cu-MIL-101(Fe) were probed by pyridine IR. It shows that the Lewis acid sites and Brownian sites of Cu-MIL-101(Fe) were displayed at 1450 cm^{-1} and 1550 cm^{-1} , respectively, and the peak intensity of Lewis acid increased with increasing Cu doping (Fig. 2d) [34,35]. This means that the doping of Cu leads to the formation of Lewis acid sites, which is beneficial to the adsorption and reaction of PS (alkaline oxidant) [36]. Electrochemical impedance spectroscopy (EIS) and cyclic voltammetry (CV) were used to investigate the electrochemical properties (Fig. 2e and f). A smaller semicircular arc and a larger area were observed, indicating that Cu-MIL-101(Fe) has a faster electron transfer rate [37]. This could be attributed to the promotion of electron transfer by the DEEF, thereby exhibiting higher electrochemical activity. The symmetry of the CV morphology suggests that the electron transfer is reversible. The decrease in fluorescence intensity of Cu-MIL-101(Fe) also confirms that electrons can migrate rapidly under the action of a DEEF (Fig. S3d). These results suggest that IMEF can greatly improve interfacial electrochemical properties, which may favor catalytic behavior.

3.2. Catalytic performance and ROS

The role of IMEF in Cu-MIL-101(Fe) is expected to profoundly affect its catalytic behavior. Using the typical AP (BPA) as the model pollutant. The PS catalysis and pollutant removal ability of Cu-MIL-101(Fe) were quite different (Fig. S4a and b). Within 30 min of adsorption, the removal of BPA was within 25%. Cu-MIL-101(Fe)-5 (0.21548 min^{-1}) exhibited higher PS catalytic kinetics than MIL-101(Fe) (0.01048 min^{-1}), a 20.6-fold improvement (Fig. 3a). It surpasses the results that reported for FeMOF under similar conditions (Table S3). The stability of catalytic degradation in an aqueous environment is critical. Cu-MIL-101(Fe) can maintain more than 90% BPA removal after ten times cycling usage (Fig. S4c). XRD and XPS results also verified that the crystal structure and chemical composition of Cu-MIL-101(Fe) did not change significantly after cycling (Fig. S4d and e). Only a small number of ions are leached during the reaction (Fig. S4f). However, ion leaching solution cannot effectively catalyze the degradation of BPA by PS (Fig. S4g), the mixture of MIL-101(Fe) and Cu ions (according to inductive coupled plasma emission spectrometer (ICP), Cu content is 32.06 mg/g in Cu-MIL-101(Fe)-5) could only remove a small amount of BPA (Fig. S4h). This demonstrates the heterogeneous catalysis of Cu-MIL-101(Fe)-5. This is not only attributed to the improved electronic structure due to Cu doping but is more likely related to the interfacial reaction regulated by the IMEF, which thereby regulates the targeting degradation efficiency and excellent stability.

The ROS of the reaction is a critical part of in the efficient interfacial catalysis process. The removal of BPA was significantly inhibited by tert-butanol (TBA) and methanol (MeOH). It is indicated that $\text{SO}_4^{\cdot -}$ contributed more than 95% to the removal of BPA. While OH usually comes from the conversion of $\text{SO}_4^{\cdot -}$ in the PS system (Fig. S5a) [38,39]. The presence of $\text{SO}_4^{\cdot -}$ was detected by electron paramagnetic resonance (EPR), which also confirmed that $\text{SO}_4^{\cdot -}$ was the main ROS responsible for the degradation of BPA (Fig. S5b and c). Oxidation products (p-hydroxybenzoic acid) of molecular probes (benzoic acid, BA) were used for the quantification of OH and $\text{SO}_4^{\cdot -}$ [40]. Cu-MIL-101(Fe) exhibited 10 times more $\text{SO}_4^{\cdot -}$ generation potency than MIL-101(Fe), which is similar to the results of catalytic performance (Fig. S5d). The additional and enhanced catalytic kinetics may be attributed to the impact of the IMEF on the regulation of $\text{SO}_4^{\cdot -}$ migration.

High oxidant utilization has been a critical indicator for superior Fenton-like systems. The continuous and efficient generation of $\text{SO}_4^{\cdot -}$ and OH was detected in Cu-MIL-101(Fe)/PS system (Fig. S5d). It is different from the Fenton reagent ($\text{C}(\text{FeSO}_4)=\text{C}(\text{Cu-MIL-101(Fe)})$) detected transient and massive radicals. According to the PS consumption, the effective utilization of PS was calculated to be 73.54% (Cu-MIL-101(Fe)) and 17.12% (Fe^{2+}) (Fig. 3c). These results show that Cu-MIL-101(Fe)-5 achieves a very high PS utilization rate, which is 4.3 times higher than that of the Fenton reagent. It demonstrates the superiority of this electronic structure improvement and IMEF regulation strategy for designing efficient Fenton-like systems.

To elucidate the generation mechanism of highly effective oxidant availability, the role of BPA in the interfacial process was first investigated. It has been reported that the presence of organic pollutants may promote the decomposition of PS, which may be attributed to the cation- π interaction, π - π conjugation, electrostatic interactions, and hydrogen bonding between the pollutants and catalysts [17,41]. The results showed that the presence of BPA increased the consumption of PS (Fig. 3b). This was further confirmed by the EPR result, where the presence of BPA significantly enhanced the $\text{SO}_4^{\cdot -}$ and OH signals (Fig. 3d). And in the absence of PS, the interaction of Cu-MIL-101(Fe) with BPA also resulted in a small amount of OH production (Fig. 3d). These implies that the interaction of Cu-MIL-101(Fe) with BPA can produce a strong reduction effect to promote the redox cycle, probably because the electron-donating effect of BPA promotes selective catalytic reduction [42].

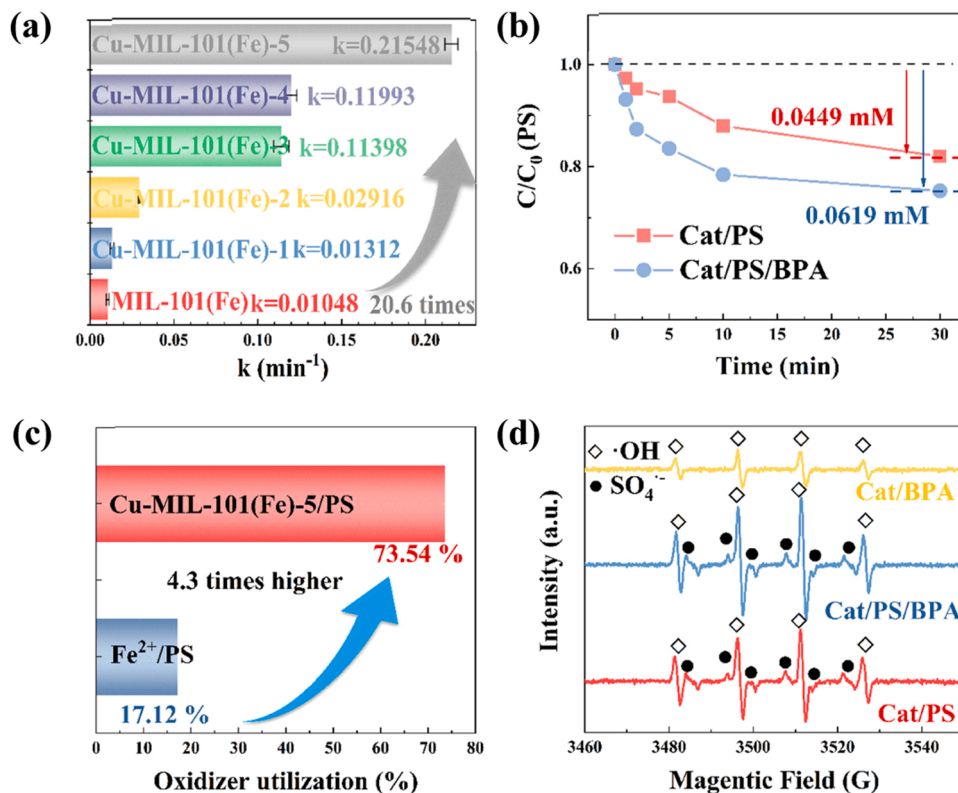


Fig. 3. (a) kinetic reaction rate constant of Cu-MIL-101(Fe); (b) PS consumption; (c) effective utilization of PS; (d) EPR of Cu-MIL-101(Fe)-5. Experimental conditions: initial BPA concentration = 0.005 mM, initial PS concentration = 0.25 mM, catalyst dosage = 1.0 g/L, pH = 4.3 ± 0.2 , temperature = 15 °C.

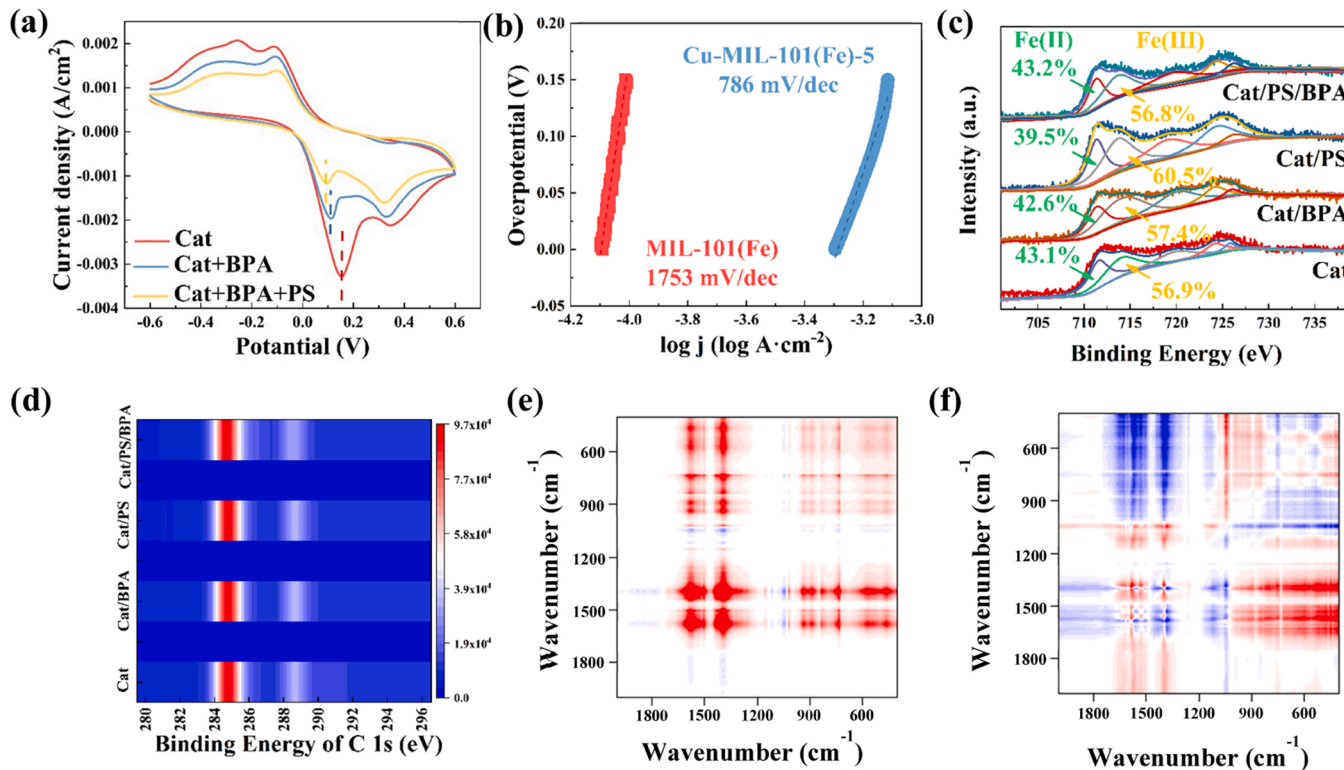


Fig. 4. (a) CV of Cu-MIL-101(Fe)-5; (b) Tafel curve in BPA solutions; (c) XPS Fe 2p; (d) XPS C 1s; (e) synchronous and (f) asynchronous spectra of 2D-FTIR-COS.

3.3. Interface behavior mechanism

The unique interfacial mechanism is critical in leading to this excellent catalytic behavior and highly effective oxidant utilization. The interaction of BPA with Cu-MIL-101(Fe) was analyzed by CV. As shown in Fig. 4a, the lower oxidation potential of Cu-MIL-101(Fe) was observed as BPA was added to the system. This result was also authenticated by linear sweep voltammetry (LSV) detection results which are shown in Fig. S6a. This indicates that the presence of BPA considerably lowers the electron transfer potential on the catalyst surface. Notably, the electrochemical impedance increased significantly when small amounts of PS and BPA were added, which describes the electron transfer rate change for Cu-MIL-101(Fe) (Fig. S6b). These results suggest that the interaction of BPA on the surface of Cu-MIL-101(Fe) could induce electron transfer [43]. Combined with the EPR and molecular probes results, it can be found that a small number of free radicals, such as $\text{SO}_4^{\cdot-}$ and OH^{\cdot} were produced in the presence of BPA alone (Fig. S6c). Similar CV and LSV signals were also observed as the other pollutants (Fig. S6d and e), such as bisphenol AF (BPAF), diclofenac sodium (DCF), tetracycline hydrochloride (TTCH), and rhodamine B (RhB) were added, implying that a variety of AP could be interacted on the surface of the catalyst to induce electron transfer.

The interaction of AP with Cu-MIL-101(Fe) is a direct electron transfer process that is triggered by AP on the surface of Cu-MIL-101(Fe). Furthermore, the Tafel slope was used to study the interaction of AP on the Cu-MIL-101(Fe) surface (Fig. S6f). The slope can be used to intuitively represent the number of electrons that transformed during the interaction process [44]. The Tafel slope of Cu-MIL-101(Fe) – 5 was much lower than that of MIL-101(Fe) (Fig. 4b), which indicated that Cu-MIL-101(Fe) had a stronger electron transfer ability than MIL-101(Fe) for BPA oxidation. This may be due to the IMEF mediated electron transfer, which promotes charge cycling on the Cu site for continuous adsorption and binding of BPA. It implies the improved electronic structure of Cu-MIL-101(Fe) and the regulation strategy of the IMEF, making it easier to obtain electrons from AP [20]. CV also showed a lower oxidation peak potential of Cu-MIL-101(Fe) – 5, indicating that it has a stronger electron transfer ability than MIL-101(Fe) for BPA oxidation (Fig. S6g). These results provide evidence that the cation- π on

Cu of Cu-MIL-101(Fe) interacts with AP and that AP can act as an electron donor and thus selectively catalyze the efficient conversion of PS to $\text{SO}_4^{\cdot-}$.

To further decipher the mechanism of IMEF modulation, the surface electronic properties of the catalysts were examined next, especially the main reaction sites of Fe sites and Cu sites for PS catalysis and BPA adsorption. Fig. 4c depicted the average valence variation of Fe via Fe 2p analysis from XPS detection results. It can be concluded that the existence of PS in the reaction system can increase the average valence of Fe, while those of BPA can decrease the average valence of Fe. Changes of Fe-O and Cu-O in the reaction with PS alone were analyzed by FTIR (Fig. S7a). The results of 2D-FTIR-COS show that the peak of Fe-O changes before the Cu-O peak and organic ligands peak during the reaction with PS (Fig. S7b and c). This implies that Fe participates in the reaction before Cu and organic ligands, confirming that Fe is the main catalytic site for PS reduction. XPS C 1 s test results showed no significant change in binding energy after the reaction with PS and BPA (Figs. S7d and 4d). This implies that the main source of electrons supporting the redox of Fe sites is not the organic ligand, and it is not the organic ligand sites that interact with BPA. The SCN^- inhibit results showed that the adsorption of BPA is significantly reduced due to the SCN^- inhibit metal sites (Fig. S7e). This suggests that metal sites rather than organic ligands are the main sites for the adsorption and interaction of BPA. Further, the reaction of PS and BPA showed a similar valence change rule to that of Fe 2p analysis in the results of Cu 2p, implying that the Cu site directly or indirectly participated in the reaction of PS or BPA (Fig. S7f). 2D-FTIR-COS analysis results indicate that Cu-O changes first before Fe-O and organic ligands during the reaction with BPA alone (Figs. S7g, 4e, and f). This means that Cu interacts with BPA and takes electrons from BPA, further confirming the cation- π interaction between Cu and BPA. The electrons captured at the Cu site from BPA are transported to the Fe site via DEEF, facilitating the redox cycle and thus enhancing the conversion of PS to $\text{SO}_4^{\cdot-}$. Fig. 5a-c shows the PS's fully relaxed atomic configuration on Cu-MIL-101(Fe). PS is cleaved at Fe sites adjacent to Cu sites, but not at both Cu sites and Fe sites far from Cu sites. This indicates that only the adjacent Fe sites under the influence of Cu can effectively cleave PS, embodying the crucial role of IMEF [45]. The results of the differential charge density showed that the cleavage of

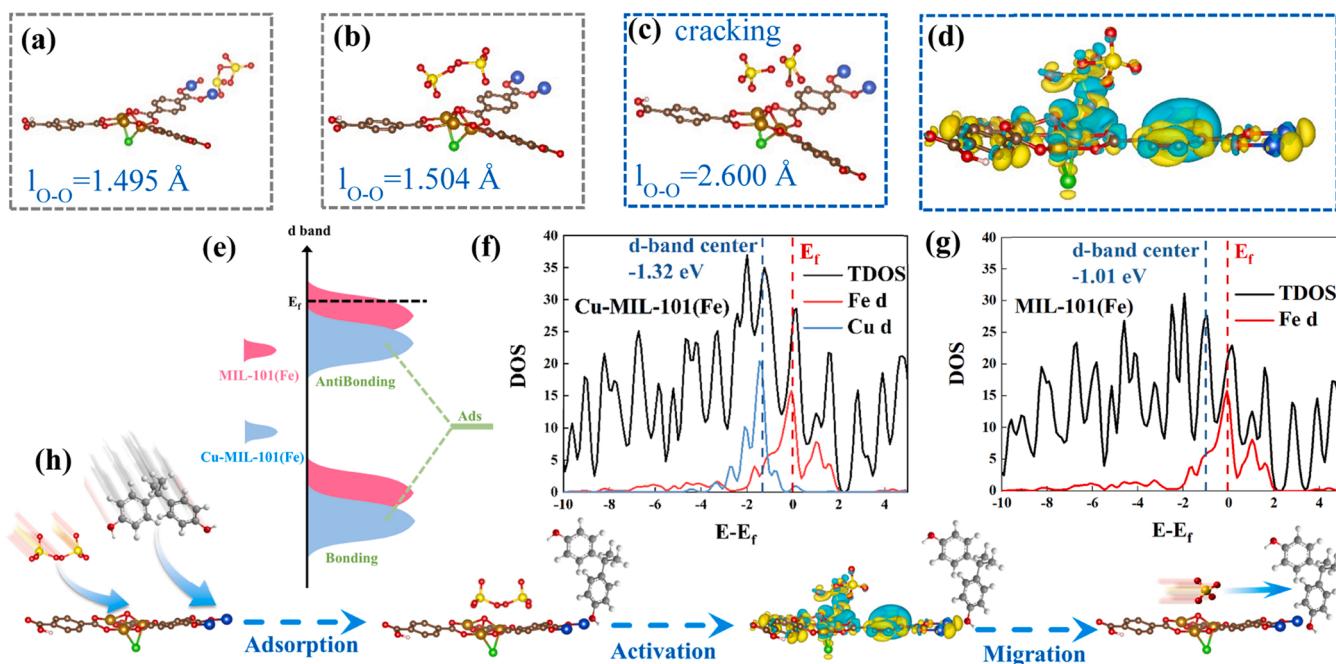


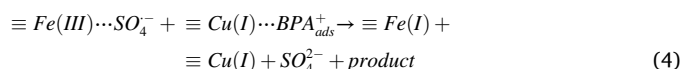
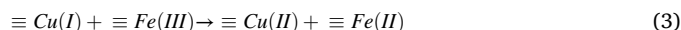
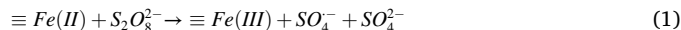
Fig. 5. (a-c) Adsorption model of PS on Cu-MIL-101(Fe); (d) differential charge density of PS adsorbed on Cu-MIL-101(Fe); (e) adsorption energy of PS; density of states of (f) MIL-101(Fe) and (g) Cu-MIL-101(Fe); (h) possible interface reaction mechanism.

PS at the Fe site is an electron-gaining process, which further supports the conclusion that the PS at the Fe site was catalytically reduced to produce SO_4^- (Fig. 5d).

The molecular mechanism by which IMEF regulation enhances catalysis was further elucidated by DFT calculations. The fast electron transfer is fundamentally derived from the improvement of electronic structure. According to the electron density of states analysis, MIL-101 (Fe) still maintains the metallicity. In the presence of Cu 3d, more orbitals cross the Fermi level (Fig. 5f and g). It indicates the metallicity of Cu-MIL-101(Fe) is stronger than MIL-101(Fe) for improved electron mobility [46]. Furthermore, Fe 3d is much more distributed at the Fermi level than Cu 3d, indicating that Fe has better electron mobility than Cu. It also benefits from the strong superexchange interaction of Fe...Cu. Combined with XPS, FTIR, and adsorption models of DFT, it further confirms that Fe is the catalytic site of PS. More importantly, the d-band center shifted from -1.01 eV to -1.31 eV after Cu introduction. This may be due to the effect of Cu 3d orbital hybridization on the broadening of the d orbital, which leads to the shift of the d band center to the lower energy level. It would pull down the bonding and antibonding orbitals (Fig. 5e). As a result, the adsorption of reactive oxygen intermediates may be weakened, thereby favoring the desorption and migration of SO_4^- [47,48].

In conclusion, IMEF regulation plays a crucial role in targeted degradation. Based on experiments, characterizations, and theoretical calculations, the possible mechanism is proposed: (I) Cu site enrich BPA at the interface, and abstract electrons from BPA through cation- π interaction [20]; (II) DEEF mediates strong superexchange interaction of Fe...Cu, promoting the transfer of e^- from the Cu site to the Fe site, accelerates the redox cycle to selectively catalyzes PS to produce SO_4^- ; (III) DIEF mediates the targeted migration of SO_4^- from the Fe site to the Cu site at the interface, thereby targeting the degradation of BPA. The IMEF mediated the multi-step tandem reaction of catalyzing PS. More importantly, the directional migration of SO_4^- was confined and

regulated by the confinement effect of the DIEF, to facilitate the near-surface adsorbed BPA targeted degradation (Fig. 5h, Eqs. (1)–(4)). This may be an important clue and mechanism for the confinement effect of IMEF to modulate the directional migration of SO_4^- .



3.4. Removal of organic pollutants in the complex aqueous environment

The removal of pollution in the actual aqueous environment is affected by many complex factors. The effects of pH, humic acid (HA), and actual water bodies were studied to assess the utility of the system. Less than 20% difference in BPA removal by Cu-MIL-101(Fe)/PS at pH 3–11 (Fig. S8a and b). This may be due to the formation of an acidic microenvironment within the catalyst near-surface Stern electric layer. It has been reported that the chemical reaction changes most significantly in the nano-confined space [14]. The concentration of counter ions (protons) in the negatively charged surface Stern electric layer in the nanoconfinement increases. This means that the H^+ concentration near the surface of the MOFs will be much higher than the average concentration. Cu-MIL-101(Fe) aggregates PS and BPA near the interface locally so that it is less affected by the ions in the solution. The comparison experiments in the buffer salt system confirm this, Cu-MIL-101(Fe) still maintains a higher catalytic activity in the alkaline buffer salt environment compared to Fe^{2+} /PS and Cu^+ /PS (Fig. 6a). In addition, HA had little effect (<5%) on the removal rate of BPA (Fig. S8c). In the real water environment (Yangtze River water), natural

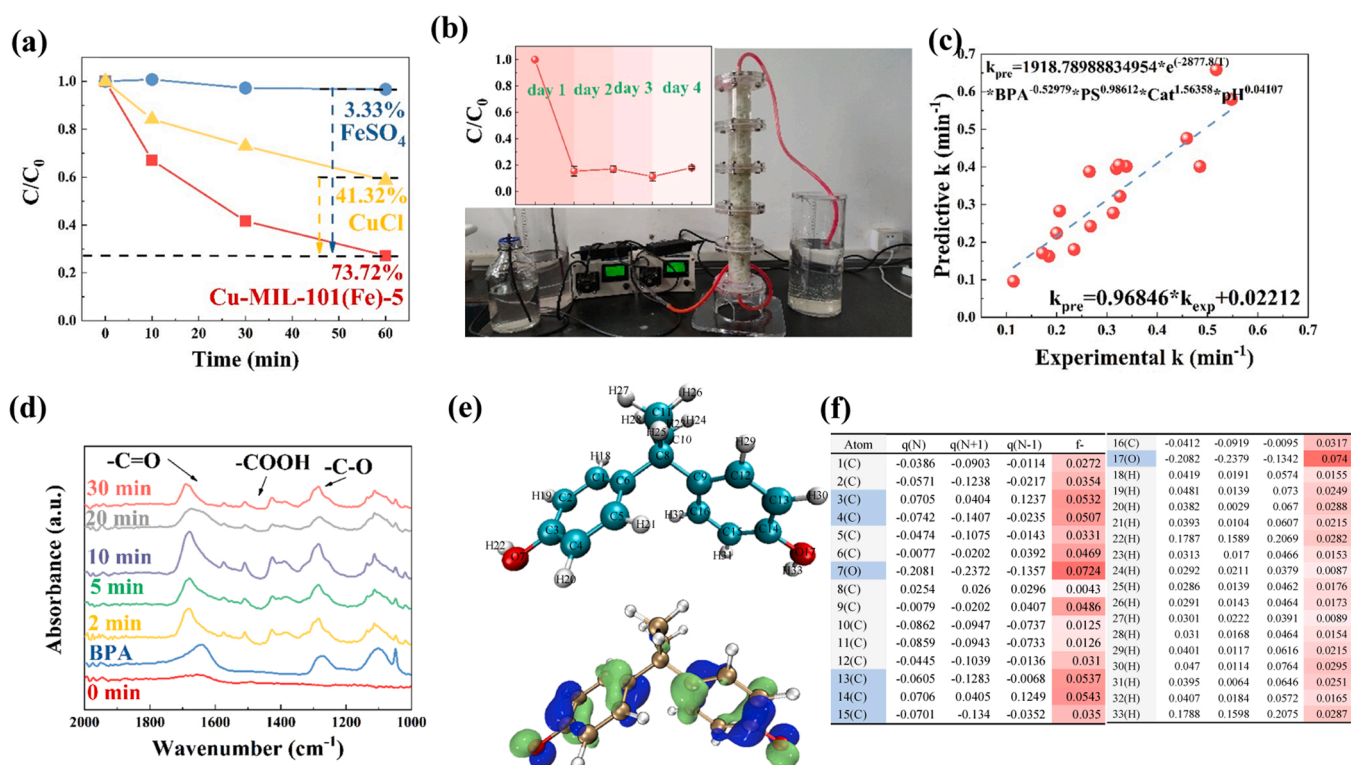


Fig. 6. (a) Control experiment under buffer salt system (10 mM borate buffer, pH 8.93); (b) the continuous flow reactor and performance; (c) kinetic model analysis kinetic prediction values; (d) in situ ATR-FTIR of Cu-MIL-101(Fe)-5/PS/BPA solution; (e) chemical structure and HOMO of BPA; (f) NPA charge distributions and Fukui index (f^-) of BPA.

organic matter, soluble microorganisms, and complex substances in the water may all have side effects. The three-dimensional fluorescence spectrum shows that the characteristic peaks of NOM and BPA after the reaction are weakened (Fig. S8d and e). This indicates that Cu-MIL-101 (Fe) also has good performance in the real water environment and is less affected by the macroscopic water environment, due to the acidic confinement micro-environment formed by the IMEF [49,50].

Experimental conditions: initial BPA concentration = 0.005 mM, initial PS concentration = 0.25 mM, catalyst dosage = 1.0 g/L, pH = 4.3 ± 0.2 , temperature = 15 °C.

The continuous operation in the reactor is an important indicator to test the practical application ability of the Fenton-like system. A pilot plant was designed as shown in Fig. 6b, the reactor consists of a catalytic tower loaded with Cu-MIL-101(Fe) loaded cotton felt and a simulated wastewater container. The mixture of BPA and PS was continuously fed into the reaction (Hydraulic retention time is designed to be 60 min). The long-term operation results show that the removal rate of BPA is stable above 80%, which confirms the potential of Cu-MIL-101(Fe) in practical applications. The reaction parameters were further investigated to optimize the process. Increasing catalyst concentration, PS concentration and temperature would increase the kinetic reaction rate (Fig. S9a-f). Increasing BPA concentration would decrease the kinetic reaction rate (Fig. S9g and h). Kinetic models were established based on statistical fitting of kinetic parameters (catalyst concentration, PS concentration, BPA concentration, pH, temperature) based on the Arrhenius equation (Eqs. (5) and (6)). The predicted and experimental values show a good correlation (Fig. 6c). This could provide theoretical guidance for optimizing the Fenton-like system's operating parameters.

$$k_{\text{predict}} = 0.96846 \times k_{\text{experiment}} + 0.02212 \quad (5)$$

$$k_{\text{predict}} = 1918.78988e^{\frac{1}{RT}} \text{BPA}^{-0.52979} \text{PS}^{0.98612} \text{Cat}^{1.56358} \text{pH}^{0.04107} \quad (6)$$

IMEF mediated $\text{SO}_4^{\cdot-}$ directed migration in a confined microenvironment achieves rapid targeted degradation. In situ ATR-FTIR was used to preliminarily observe the oxidation process of BPA on the surface of Cu-MIL-101(Fe). The peaks located at 1673 cm^{-1} , 1482 cm^{-1} , and 1194 cm^{-1} can be assigned to $\text{C}=\text{O}$, -COOH , C-O , etc., respectively (Fig. 6d). This means that BPA on the catalyst surface is oxidatively degraded into other products, which in turn continue to react and eventually convert into CO_2 and H_2O . Degradation products were analyzed by LC-MS (Fig. S10 and Table S4). Due to the influence of adjacent groups and elements, the electronic states of different atoms of BPA and degradation products are different. The highest occupied orbital (HOMO level) and lowest unoccupied orbital (LUMO) of BPA and degradation products were analyzed (Fig. 6e). The calculation results of the Fukui function and the dual descriptor are shown in Fig. 6e and f. Specifically, $f(-)$ shows that the C3, C4, O7, C13, C14, C15, and O17 sites are vulnerable to free radical attack [51]. Based on this, a possible degradation pathway was hypothesized (Fig. S11a), bicyclic organic compounds such as BPA are gradually broken into monocyclic products, which are further mineralized by ring-opening. The acute toxicity of BPA and its degradation products was assessed by the Toxicity Evaluation Software Tool (TEST). Acute toxicity was assessed by LC_{50} of Fathead minnow (96 h) (concentration causing 50% death of Fathead minnow at 96 h) and LC_{50} of *Daphnia magna* (48 h) (concentration causing 50% death of *Daphnia magna* at 48 h) [52]. The predicted results showed that some less toxic and harmless products were produced after BPA degradation (Fig. S11b and c). These results showed that the acid confinement microenvironment formed by the IMEF could reduce degradation products and pathways, avoiding the formation of highly toxic products, and enabling rapid mineralization and detoxification.

4. Conclusion

In summary, an efficient Cu-MIL-101(Fe) catalyst was successfully

constructed, which for the first time was exploited to control $\text{SO}_4^{\cdot-}$ generation, release, and directional migration by optimizing the electronic structure. The increased distribution of d occupied orbitals at the Fermi level means that the metallicity is enhanced, which is beneficial to electron transfer and promotes the selective generation of $\text{SO}_4^{\cdot-}$. The Cu 3d orbital hybridization leads to the displacement of the d-band center to the lower energy level, which promotes the desorption and release of $\text{SO}_4^{\cdot-}$. The directional migration of $\text{SO}_4^{\cdot-}$ is regulated by the IMEF formed by the intramolecular charge offset. The strong superexchange interaction ensures the stability of IMEF and continuous water purification. Compared with homogeneous Fe^{2+} , the effective utilization of oxidant is increased by 4.3 times (from 17.12% to 73.54%). The long-term operational stability has been verified by the pilot plant. In addition, compared with previous studies, the confinement effect of IMEF confines the interfacial reaction of ROS within the near-surface Stern electric layer, forming an acidic microenvironment less affected by pH, salt ions, etc. This work provides a new idea for regulating ROS's release and directional migration for efficient catalytic reactions. The findings here may lay the foundation for guiding the rational design of catalysts for efficient and selective catalytic processes.

CRediT authorship contribution statement

Dongya Li: Formal analysis, Investigation, Writing – original draft, Visualization, Funding acquisition, Data curation. **Shiyu Zuo:** Conceptualization, Methodology, Formal analysis, Investigation, Writing – original draft, Writing – review & editing, Visualization, Data curation. **Jinquan Wan:** Funding acquisition, Project administration. **Yan Wang:** Data curation, Validation, Writing – review & editing, Formal analysis, Project administration. **Zeyu Guan:** Funding acquisition. **Zhicheng Yan:** Supervision. **Fan Yang:** Visualization, Theoretical calculations.

Declaration of Competing Interest

The authors declare that they have no known competing financial interests or personal relationships that could have appeared to influence the work reported in this paper.

Data availability

Data will be made available on request.

Acknowledgments

This work was supported by the National Key Research and Development Program of China (No. 2018YFE0110400), the National Natural Science Foundation of China (No. 21978102), the Central Government Guidance for Local Science and Technology Development Projects for Hubei Province (No. 2020ZYD038) and Natural Science Foundation of Guangdong Province (No. 2023A1515011186).

Appendix A. Supplementary material

Supplementary data associated with this article can be found in the online version at doi:10.1016/j.apcatb.2023.122507.

References

- [1] J. Yu, Z. Zhu, H. Zhang, Y. Qiu, D. Yin, Fe–nitrogen–doped carbon with dual active sites for efficient degradation of aromatic pollutants via peroxymonosulfate activation, *Chem. Eng. J.* 427 (2022), 130898.
- [2] L. Lyu, L. Zhang, Q. Wang, Y. Nie, C. Hu, Enhanced Fenton catalytic efficiency of $\gamma\text{-Cu-Al}_2\text{O}_3$ by $\sigma\text{-Cu}^{2+}$ -ligand complexes from aromatic pollutant degradation, *Environ. Sci. Technol.* 49 (2015) 8639–8647.
- [3] Z. Yang, Y. Shi, H. Li, C. Mao, X. Wang, X. Liu, X. Liu, L. Zhang, Oxygen and chlorine dual vacancies enable photocatalytic O_2 dissociation into monatomic reactive oxygen on BiOCl for refractory aromatic pollutant removal, *Environ. Sci. Technol.* 56 (2022) 3587–3595.

- [4] H. Zhang, C. Li, L. Lyu, C. Hu, Surface oxygen vacancy inducing peroxymonosulfate activation through electron donation of pollutants over cobalt-zinc ferrite for water purification, *Appl. Catal. B Environ.* 270 (2020), 118874.
- [5] M. Ekblad, P. Falas, H. El-Taliawy, F. Nilsson, K. Bester, M. Hagman, M. Cimbritz, Is dissolved COD a suitable design parameter for ozone oxidation of organic micropollutants in wastewater? *Sci. Total Environ.* 658 (2019) 449–456.
- [6] A.K.E. Terechovs, A.J. Ansari, J.A. McDonald, S.J. Khan, F.I. Hai, N.A. Knott, J. Zhou, L.D. Nghiem, Occurrence and bioconcentration of micropollutants in Silver Perch (*Bidyanus bidyanus*) in a reclaimed water reservoir, *Sci. Total Environ.* 650 (2019) 585–593.
- [7] J. Lee, U. Von Gunten, J.-H. Kim, Persulfate-based advanced oxidation: critical assessment of opportunities and roadblocks, *Environ. Sci. Technol.* 54 (2020) 3064–3081.
- [8] G.P. Anipsitakis, D.D. Dionysiou, M.A. Gonzalez, Cobalt-mediated activation of peroxymonosulfate and sulfate radical attack on phenolic compounds. implications of chloride ions, *Environ. Sci. Technol.* 40 (2006) 1000–1007.
- [9] Q. He, J.-J. Liang, L.-X. Chen, S.-L. Chen, H.-L. Zheng, H.-X. Liu, H.-J. Zhang, Removal of the environmental pollutant carbamazepine using molecular imprinted adsorbents: molecular simulation, adsorption properties, and mechanisms, *Water Res.* 168 (2020), 115164.
- [10] X. Li, J. Wan, Y. Wang, Z. Yan, H. Chi, S. Ding, Mechanism of accurate recognition and catalysis of diethyl phthalate (DEP) in wastewater by novel MIL100 molecularly imprinted materials, *Appl. Catal. B Environ.* 266 (2020), 118591.
- [11] Y. Xie, J. Wan, Z. Yan, Y. Wang, T. Xiao, J. Hou, H. Chen, Targeted degradation of sulfamethoxazole in wastewater by molecularly imprinted MOFs in advanced oxidation processes: degradation pathways and mechanism, *Chem. Eng. J.* 429 (2022), 132237.
- [12] X. Li, B. Yang, K. Xiao, H. Duan, J. Wan, H. Zhao, Targeted degradation of refractory organic compounds in wastewaters based on molecular imprinting catalysts, *Water Res.* 203 (2021), 117541.
- [13] X. Li, J. Wan, Y. Wang, S. Ding, J. Sun, Improvement of selective catalytic oxidation capacity of phthalates from surface molecular-imprinted catalysis materials: design, mechanism, and application, *Chem. Eng. J.* 413 (2021), 127406.
- [14] S. Zhang, M. Sun, T. Hedtke, A. Deshmukh, X. Zhou, S. Weon, M. Elimelech, J.-H. Kim, Mechanism of heterogeneous fenton reaction kinetics enhancement under nanoscale spatial confinement, *Environ. Sci. Technol.* 54 (2020) 10868–10875.
- [15] X. Pan, X. Bao, The effects of confinement inside carbon nanotubes on catalysis, *Acc. Chem. Res.* 44 (2011) 553–562.
- [16] L. Tang, X. Meng, D. Deng, X. Bao, Confinement catalysis with 2D materials for energy conversion, *Adv. Mater.* 31 (2019) 1901996.
- [17] M. Tang, J. Wan, Y. Wang, Z. Yan, Y. Ma, J. Sun, S. Ding, Developing a molecularly imprinted channels catalyst based on template effect for targeted removal of organic micropollutants from wastewaters, *Chem. Eng. J.* 445 (2022), 136755.
- [18] X. Huang, C. Tang, J. Li, L.-C. Chen, J. Zheng, P. Zhang, J. Le, R. Li, X. Li, J. Liu, Electric field-induced selective catalysis of single-molecule reaction, *Sci. Adv.* 5 (2019) eaaw3072.
- [19] S. Zuo, D. Li, Z. Guan, F. Yang, J. Song, H. Xu, D. Xia, H. Li, X. Li, A directional Built-in electric field mediates the electron transfer synergy mechanism of the radical/nonradical pathway in FeOCl-CuO, *Chem. Eng. J.* 430 (2022), 133004.
- [20] K. Deng, Y. Gu, T. Gao, Z. Liao, Y. Feng, S. Zhou, Q. Fang, C. Hu, L. Lyu, Carbonized MOF-coated zero-valent Cu driving an efficient dual-reaction-center fenton-like water treatment process through utilizing pollutants and natural dissolved oxygen, *ACS ES&T Water* 2 (2022) 174–183.
- [21] Q. Zhao, X.-H. Yi, C.-C. Wang, P. Wang, W. Zheng, Photocatalytic Cr(VI) reduction over MIL-101(Fe)-NH₂ immobilized on alumina substrate: from batch test to continuous operation, *Chem. Eng. J.* 429 (2022), 132497.
- [22] Q. Zhao, C.-C. Wang, P. Wang, Effective norfloxacin elimination via photo-Fenton process over the MIL-101(Fe)-NH₂ immobilized on α -Al₂O₃ sheet, *Chin. Chem. Lett.* 33 (2022) 4828–4833.
- [23] X. Ren, C.-C. Wang, Y. Li, P. Wang, S. Gao, Defective SO₃H-MIL-101(Cr) for capturing different cationic metal ions: performances and mechanisms, *J. Hazard. Mater.* 445 (2023), 130552.
- [24] Q. Yan, C. Lian, K. Huang, L. Liang, H. Yu, P. Yin, J. Zhang, M. Xing, Constructing an acidic microenvironment by MoS₂ in heterogeneous Fenton reaction for pollutant control, *Angew. Chem.* 133 (2021) 17292–17300.
- [25] Y. Jiang, Z. Wang, J. Huang, F. Yan, Y. Du, C. He, Y. Liu, G. Yao, B. Lai, A singlet oxygen dominated process through photocatalysis of CuS-modified MIL-101 (Fe) assisted by peroxymonosulfate for efficient water disinfection, *Chem. Eng. J.* 439 (2022), 135788.
- [26] J. Han, Y. Wang, J. Wan, Y. Ma, Catalytic hydrolysis of cellulose by phosphotungstic acid-supported functionalized metal-organic frameworks with different electronegative groups, *Environ. Sci. Pollut. Res.* 26 (2019) 15345–15353.
- [27] J. Sun, J. Wan, Y. Wang, Z. Yan, Y. Ma, S. Ding, M. Tang, Y. Xie, Modulated construction of Fe-based MOF via formic acid modulator for enhanced degradation of sulfamethoxazole: design, degradation pathways, and mechanism, *J. Hazard. Mater.* (2022), 128299.
- [28] Y. Wan, J. Wan, Y. Ma, Y. Wang, T. Luo, Sustainable synthesis of modulated Fe-MOFs with enhanced catalyst performance for persulfate to degrade organic pollutants, *Sci. Total Environ.* 701 (2020), 134806.
- [29] S. Zuo, Z. Guan, D. Xia, F. Yang, H. Xu, M. Huang, D. Li, Polarized heterogeneous CuO-CN for peroxymonosulfate nonradical activation: An enhancement mechanism of mediated electron transfer, *Chem. Eng. J.* 420 (2021), 127619.
- [30] L. Ding, R. Mao, S. Ma, X. Guo, L. Zhu, High temperature depended on the ageing mechanism of microplastics under different environmental conditions and its effect on the distribution of organic pollutants, *Water Res.* 174 (2020), 115634.
- [31] H. Chen, Q. Li, M. Wang, D. Ji, W. Tan, XPS and two-dimensional FTIR correlation analysis on the binding characteristics of humic acid onto kaolinite surface, *Sci. Total Environ.* 724 (2020), 138154.
- [32] J. Low, B. Dai, T. Tong, C. Jiang, J. Yu, In situ irradiated X-ray photoelectron spectroscopy investigation on a direct Z-scheme TiO₂/CdS composite film photocatalyst, *Adv. Mater.* 31 (2019) 1802981.
- [33] S. Zuo, Z. Guan, F. Yang, D. Xia, D. Li, Reactive oxygen species regulation and synergistic effect for effective water purification through Fenton-like catalysis on single-atom Cu-N sites, *J. Mater. Chem. A* 10 (2022) 10503–10513.
- [34] J. Yang, S. Hu, L. Shi, S. Hoang, W. Yang, Y. Fang, Z. Liang, C. Pan, Y. Zhu, L. Li, Oxygen vacancies and lewis acid sites synergistically promoted catalytic methane combustion over perovskite oxides, *Environ. Sci. Technol.* 55 (2021) 9243–9254.
- [35] Z. Shen, X. Liu, S. Impeng, C. Zhang, T. Yan, P. Wang, D. Zhang, Alkali and heavy metal copoisoning resistant catalytic reduction of NO_x via liberating Lewis acid sites, *Environ. Sci. Technol.* (2022).
- [36] H. Zeng, L. Deng, L. Yang, H. Wu, H. Zhang, C. Zhou, B. Liu, Z. Shi, Novel Prussian blue analogues@MXene nanocomposite as heterogeneous activator of peroxymonosulfate for the degradation of coumarin: the nonnegligible role of Lewis-acid sites on MXene, *Chem. Eng. J.* 416 (2021), 128071.
- [37] H. Wang, W. Guo, B. Liu, Q. Wu, H. Luo, Q. Zhao, Q. Si, F. Sseguya, N. Ren, Edgennitrogenated biochar for efficient peroxydisulfate activation: an electron transfer mechanism, *Water Res.* 160 (2019) 405–414.
- [38] G.V. Buxton, C.L. Greenstock, W.P. Helman, A.B. Ross, Critical review of rate constants for reactions of hydrated electrons, hydrogen atoms and hydroxyl radicals ($\cdot\text{OH}/\cdot\text{O}^-$ in aqueous solution), *J. Phys. Chem. Ref. Data* 17 (1988) 513–886.
- [39] P. Neta, R.E. Huie, A.B. Ross, Rate constants for reactions of inorganic radicals in aqueous solution, *J. Phys. Chem. Ref. Data* 17 (1988) 1027–1284.
- [40] S.X. Liang, Z. Jia, W.C. Zhang, X.F. Li, W.M. Wang, H.C. Lin, L.C. Zhang, Ultrafast activation efficiency of three peroxides by Fe₇Si₉B₁₃ metallic glass under photo-enhanced catalytic oxidation: a comparative study, *Appl. Catal. B Environ.* 221 (2018) 108–118.
- [41] S. Zhan, H. Zhang, X. Mi, Y. Zhao, C. Hu, L. Lyu, Efficient Fenton-like process for pollutant removal in electron-rich/poor reaction sites induced by surface oxygen vacancy over cobalt-zinc oxides, *Environ. Sci. Technol.* 54 (2020) 8333–8343.
- [42] L. Lyu, W. Cao, G. Yu, D. Yan, K. Deng, C. Lu, C. Hu, Enhanced polarization of electron-poor/rich micro-centers over nZVCu-Cu (II)-rGO for pollutant removal with H₂O₂, *J. Hazard. Mater.* 383 (2020), 121182.
- [43] T. Gao, C. Lu, C. Hu, L. Lyu, H₂O₂ inducing dissolved oxygen activation and electron donation of pollutants over Fe-Zn quantum dots through surface electron-poor/rich microregion construction for water treatment, *J. Hazard. Mater.* 420 (2021), 126579.
- [44] W. Ren, L. Xiong, G. Nie, H. Zhang, X. Duan, S. Wang, Insights into the electron-transfer regime of peroxydisulfate activation on carbon nanotubes: the role of oxygen functional groups, *Environ. Sci. Technol.* 54 (2019) 1267–1275.
- [45] S. Zuo, Z. Guan, F. Yang, D. Xia, D. Li, Reactive oxygen species regulation and synergistic for effective water purification through fenton-like catalysis on single-atom Cu-N sites, *J. Mater. Chem. A* (2022).
- [46] M.J. Banisalman, M.-C. Kim, S.S. Han, Origin of enhanced ammonia synthesis on Ru-Co catalysts unraveled by density functional theory, *ACS Catal.* 12 (2022) 1090–1097.
- [47] C. Yang, C. Wang, L. Zhou, W. Duan, Y. Song, F. Zhang, Y. Zhen, J. Zhang, W. Bao, Y. Lu, Refining d-band center in Ni_{0.85}Se by Mo doping: a strategy for boosting hydrogen generation via coupling electrocatalytic oxidation 5-hydroxymethylfurfural, *Chem. Eng. J.* 422 (2021), 130125.
- [48] S. Sun, X. Zhou, B. Cong, W. Hong, G. Chen, Tailoring the d-band centers endows (Ni x Fe_{1-x}) 2P nanosheets with efficient oxygen evolution catalysis, *ACS Catal.* 10 (2020) 9086–9097.
- [49] M. Zhang, C. Xiao, X. Yan, S. Chen, C. Wang, R. Luo, J. Qi, X. Sun, L. Wang, J. Li, Efficient removal of organic pollutants by metal-organic framework derived Co/C yolk-shell nanoreactors: size-exclusion and confinement effect, *Environ. Sci. Technol.* 54 (2020) 10289–10300.
- [50] C. Zhu, S. Zhao, Z. Fan, H. Wu, F. Liu, Z. Chen, A. Li, Confinement of CoP nanoparticles in nitrogen-doped yolk-shell porous carbon polyhedron for ultrafast catalytic oxidation, *Adv. Funct. Mater.* 30 (2020) 2003947.
- [51] J. Qi, X. Yang, P.-Y. Pan, T. Huang, X. Yang, C.-C. Wang, W. Liu, Interface engineering of Co(OH)₂ nanosheets growing on the K₂FeO₄ perovskite based on electronic structure modulation for enhanced peroxymonosulfate activation, *Environ. Sci. Technol.* 56 (2022) 5200–5212.
- [52] Y. Wang, T. Xiao, S. Zuo, J. Wan, Z. Yan, B. Zhu, X. Zhang, Exploring degradation properties and mechanisms of emerging contaminants via enhanced directional electron transfer by polarized electric fields regulation in Fe-N₄-Cx, *J. Hazard. Mater.* 446 (2023), 130698.